



# Sensitization of 316L Stainless Steel made by Laser Powder Bed Fusion Additive Manufacturing

January 2023

*Changing the World's Energy Future*

Xiaoyuan Lou, John Snitzer



**DISCLAIMER**

This information was prepared as an account of work sponsored by an agency of the U.S. Government. Neither the U.S. Government nor any agency thereof, nor any of their employees, makes any warranty, expressed or implied, or assumes any legal liability or responsibility for the accuracy, completeness, or usefulness, of any information, apparatus, product, or process disclosed, or represents that its use would not infringe privately owned rights. References herein to any specific commercial product, process, or service by trade name, trade mark, manufacturer, or otherwise, does not necessarily constitute or imply its endorsement, recommendation, or favoring by the U.S. Government or any agency thereof. The views and opinions of authors expressed herein do not necessarily state or reflect those of the U.S. Government or any agency thereof.

# **Sensitization of 316L Stainless Steel made by Laser Powder Bed Fusion Additive Manufacturing**

**Xiaoyuan Lou, John Snitzer**

**January 2023**

**Idaho National Laboratory  
Idaho Falls, Idaho 83415**

**<http://www.inl.gov>**

**Prepared for the  
U.S. Department of Energy  
Under DOE Idaho Operations Office  
Contract DE-AC07-05ID14517**

# Sensitization of 316L Stainless Steel made by Laser Powder Bed Fusion Additive Manufacturing

John Snitzer\* and Xiaoyuan Lou<sup>‡,\*</sup>

Additively manufactured (AM) 316L stainless steel (SS) manufactured by laser powder bed fusion (L-PBF) and wrought 316L SS were subjected to sensitization heat treatments at 700°C up to 100 h. Using two evaluation methods, double-loop electrochemical potentiokinetic reactivation (DL-EPR) and ditching tests, degree of sensitization (DOS) and intergranular corrosion (IGC) susceptibility was evaluated. It was found that the wrought samples showed slightly lower IGC susceptibility compared to their AM counterpart. DOS and IGC attacks increased with sensitization time for all samples. Dislocation cellular structures were found to have little to no impact on DOS and IGC for the AM samples. Sensitized at 100 h, the AM sample showed significant Cr depletion along high-angle grain boundaries (12.35 wt% on average) and exhibited Cr carbide precipitation. Mo-rich particles along grain boundaries were also observed. The DL-EPR test attacks the surface oxide film and grain boundaries while the ditching test attacks the melt pool boundaries and grain boundaries (IGC and pitting). Changes to the DL-EPR and ditching standards for AM application have been proposed in this work.

KEY WORDS: 316L stainless steel, additive manufacturing, carbide, double-loop electrochemical potentiokinetic reactivation, intergranular corrosion, laser powder bed fusion, sensitization

## INTRODUCTION

Laser powder bed fusion (L-PBF) additively manufactured (AM) facilitates the production of complex geometry parts with minimal need for postprocessing. The layer-by-layer approach of manufacturing allows for geometrical freedom, enhanced performance, and reduced upfront production costs.<sup>1</sup> Realizing these advantages, industries such as nuclear, aerospace, and medical have adopted the technology and begun evaluating materials for specific applications. For non-critical applications, AM parts may be used with no detrimental effects; however, critical applications require extensive evaluation before implementation. Traditionally, manufactured metals have been studied for decades resulting in a significant knowledge base. Unlike their wrought counterparts, AM materials produce microstructures with heterogeneous and anisotropic features such as porosities and columnar grains with small, dendritic cellular structures forming within the grains.<sup>1-3</sup> Many of these features are caused by the extreme temperature gradient that forms because of the localized heating from the laser<sup>1-3</sup> and are heavily dependent on AM process parameters.<sup>3-7</sup>

Sensitization impacts alloys exposed to high temperatures for prolonged periods of time and corrosive environments. This phenomenon refers to the precipitation of Cr carbides along grain boundaries (GB) within the temperature range of 500°C to 800°C. As a result of the diffusion of Cr, neighboring GBs generally show Cr depletion thus making the material

susceptible to intergranular corrosion (IGC).<sup>2,8-10</sup> The alloys with higher carbon content possess a great threat of sensitization.<sup>11</sup> As such, low carbon materials such as AISI 316L stainless steel (SS) (UNS S31603<sup>(1)</sup>) have been developed to minimize the impact. 316L SS is an austenitic steel widely used for conditions where sensitization is concerning.<sup>12</sup> In the temperature range of 500°C to 800°C, M<sub>23</sub>C<sub>6</sub> tends to form along high-angle GBs (HAGB) (boundaries with misorientation angle >15°) with little to no carbides precipitating along coherent  $\Sigma$ 3 twin boundaries within low-carbon austenitic SS.<sup>11,13-15</sup> The nucleation preference of HAGBs is due to the higher energy of HAGBs compared to the lower misorientation angle boundaries.

Of the evaluation methods for the degree of sensitization (DOS), two popular tests have emerged: double-loop electrochemical potentiokinetic reactivation (DL-EPR)<sup>16</sup> and ASTM A262<sup>17</sup> practice "A" (also called "ditching test" in this work). DL-EPR tests have been extensively used for wrought austenitic SS<sup>18-21</sup> with Rebak and Dean<sup>18</sup> showing a high degree of repeatable and reproducible results among different testing laboratories. Although DL-EPR has been used for wrought materials, little work has been done on AM austenitic SS outside of the work of Macatangay, et al.,<sup>10</sup> Laleh, et al.,<sup>9</sup> and Man, et al.,<sup>22</sup> where conflicting conclusions were noted. Macatangay, et al.,<sup>10</sup> found similar IGC resistance between AM and wrought austenitic SS while Laleh, et al.,<sup>9</sup> found the AM material showed superior IGC resistance compared to its wrought counterpart due to the high percentage of twin boundaries. The ditching test has been used as a rapid screening

Submitted for publication: November 11, 2022. Revised and accepted: January 10, 2023. Preprint available online: January 10, 2023, <https://doi.org/10.5006/4241>.

<sup>‡</sup> Corresponding author. E-mail: [lou49@purdue.edu](mailto:lou49@purdue.edu).

\* School of Nuclear Engineering, Purdue University, West Lafayette, Indiana 47906.

<sup>(1)</sup> UNS numbers are listed in *Metals & Alloys in the Unified Numbering System*, published by the Society of Automotive Engineers (SAE International) and cosponsored by ASTM International.

**Table 1.** Chemical Composition of As-Built AM and Wrought 316L SS in wt%

Element	Fe	Cr	Mn	Si	Ni	Cu	Mo	C	N	S
AM 316L	Bal.	16.9	1.13	0.71	10.7	0.20	2.24	0.027	0.094	0.006
Wrought 316L	Bal.	16.6	1.52	0.39	10.0	0.47	2.00	0.021	0.038	0.002

test for many years<sup>12,20,23</sup> with Macatangay, et al.,<sup>8,10</sup> demonstrating its use for AM materials. The results showed that AM materials in the as-built condition are highly susceptible to corrosion attack by means of melt pool boundary rather than GB attack. The limited knowledge of DOS in AM materials and conflicting conclusions of previous work<sup>8-10,22</sup> require further investigation into the application and evaluation of the two testing methods for AM materials.

The objectives of this work are two-fold. The study is to provide further understanding into the use of different DOS evaluation techniques when applied to AM austenitic SS and evaluate the role of dislocation cellular structures on sensitization kinetics of AM 316L SS. Due to AM 316 SS (both high and low carbon variants) being used for intermediate or high-temperature nuclear environments, it is essential to ensure current testing methods are properly evaluating the material, otherwise, parts may be evaluated with false negatives or worse, false positives. Another objective of this work is to generate DOS data of both wrought and AM 316L and develop mechanistic understandings. Given the conflicting conclusions and lack of data, additional research is required to evaluate AM 316L for critical applications within the sensitization temperature range.

## EXPERIMENTAL PROCEDURES

### 2.1 | Materials and Manufacturing

Commercially available 316L SS powder manufactured by nitrogen gas-atomization (Carpenter Powder Products) and wrought 316L SS (Rolled Alloys, Inc.) were used in this work. The chemical composition of the two materials used was specified in Table 1. The 316L SS powder with an average size of 15  $\mu\text{m}$  to 45  $\mu\text{m}$  was used to fabricate 1.0 cm  $\times$  1.0 cm  $\times$  1.0 cm specimens with a Concept Laser Mlab LaserCusing<sup>†</sup> system with the following process parameters: 90 W laser power, 600 mm/s scan velocity, 80  $\mu\text{m}$  hatch distance, and 25  $\mu\text{m}$  layer thickness. The process parameters were predetermined for density greater than 99.7%.<sup>15</sup> The laser scan strategy consisted of a continuous laser with a 90° rotation between layers. The wrought material was received as 12.7 mm (0.5 in nominally) round stock in the solution annealed condition.

### 2.2 | Heat Treatment

Several sensitization heat treatments were applied to both AM and wrought samples. Based on previous work,<sup>8-11,22</sup> sensitization heat treatment at 700°C was chosen. The AM samples were sensitized from the as-built condition at 700°C for five different times: 0 h, 1 h, 24 h, 50 h, and 100 h. In addition to these treatments, an as-built AM sample was heat treated at 1,038°C for 10 min to recover dislocation structures within the material and subsequently heat treated at 700°C for 24 h. This specific heat treatment was designed to evaluate the contribution of dislocation cellular structures to sensitization kinetics. The wrought material was sensitized at 700°C for 0 h and 24 h

<sup>†</sup> Trade name.

for comparison. All sensitization heat treatments were followed with a water quench to prevent further sensitization during cooling. A table with all the materials and heat treatments we are found in Table 2.

### 2.3 | Material Preparation

To prepare the samples for testing, the AM parts were cut using a Buehler Isomet 2000<sup>†</sup> Precision Cutoff Saw transverse to the build direction. A 304L wire was spot welded on the back of each sample and fed through a glass tube. The glass tube acts to isolate the spot-welded wire from testing solutions and ensure no corrosion occurs on the wire. The samples were then cold mounted in Struers EpoFix<sup>†</sup> with the epoxy covering the sample, spot welded wire and at least 0.5 in of the glass tube. Before testing, specimens were polished from 120 upto 1000 grit and cleaned in an acetone bath in an ultrasonic cleaner for 5 min. Following cleaning, the testing area was isolated using 3M<sup>†</sup> 470 electroplaters tape with a 0.25 in diameter hole with sharp edges punched out. To achieve high-quality electrochemical tests, crevice corrosion must be avoided, so preliminary tests were performed to ensure little to no crevice corrosion occurred when developing sample preparation techniques.

### 2.4 | Double-Loop Electrochemical Potentiokinetic Reactivation

Once the specimens outlined in Table 2 were prepared according to the above process, they were evaluated for their DOS by means of DL-EPR according to ISO 12732.<sup>16</sup> The DL-EPR test was conducted in a 0.5 M H<sub>2</sub>SO<sub>4</sub> + 0.01 M KSCN solution deaerated with N<sub>2</sub> gas. The test was conducted with a Gamry Reference 600+<sup>†</sup> with a platinum counter electrode (CE) and saturated calomel electrode (SCE) reference electrode (RE). The CE was kept in place while the working electrode (WE) (mounted sensitized samples) was placed 0.5 in from the CE, ensuring the WE and CE were parallel. The luggin probe tip of the RE was placed as close to the WE as possible without breaking

**Table 2.** Heat-Treatment Conditions

Materials	Heat Treatment	Post Furnace
AM-AB	None (as-built condition)	None
AM-1	AM-AB + 700°C 1 h	Water quench
AM-24	AM-AB + 700°C 24 h	Water quench
AM-R-24	AM-AB + 1,038°C 10 min + 700°C 24 h	Water quench
AM-50	AM-AB + 700°C 50 h	Water quench
AM-100	AM-AB + 700°C 100 h	Water quench
W	As received	None
W-24	W + 700°C 24 h	Water quench

a direct current path to the CE. Each specimen was exposed to the solution for 30 min to obtain open-circuit potential ( $E_{\text{OCP}}$ ) and to ensure a more consistent surface oxide layer. Once OCP was reached, a potentiodynamic test was performed in the anodic direction starting at  $-100 \text{ mV}_{E_{\text{OCP}}}$  to  $+300 \text{ mV}_{\text{SCE}}$  at a scan rate of  $1.67 \text{ mV/s}$ . Once  $+300 \text{ mV}_{\text{SCE}}$  was reached, the scan direction was reversed and finished at  $-100 \text{ mV}_{E_{\text{OCP}}}$  at a scan rate of  $1.67 \text{ mV/s}$ . DOS is reported as the maximum current in the reactivation loop ( $i_r$ ) divided by the maximum current in the activation loop ( $i_a$ ). If no reactivation peak occurs, the DOS is said to be zero.

### 2.5 | Intergranular Attack Susceptibility (Ditching Test)

Tests were performed according to ASTM A262<sup>17</sup> practice "A" with both an oxalic acid and ammonium persulfate (APS) solution for comparison. All samples were prepared by the procedures outlined in *Material Preparation* section. The 10% oxalic acid and 10% APS test were conducted by etching the samples at  $1 \text{ A/cm}^2$  for 1.5 min and 5 min, respectively. Following the tests, the samples were subjected to an acetone ultrasonic cleaning for 5 min. Grain boundary attack is classified as "step," "dual," or "ditch" according to the severity of IGC. Samples with "step" or "dual" structures pass; however, samples with "ditch" structures do not pass and require further quantitative testing. It is important to note that the ditching test is not able to fail a sample, only pass it.

### 2.6 | Characterization

Following DL-EPR and ditching testing, all samples were examined by optical microscopy using a Zeiss Axiovert 10<sup>†</sup> for qualitative analysis of the grain boundary attack without further polishing. Electron backscattered diffraction (EBSD) was performed on a JEOL 7000 F<sup>†</sup> scanning electron microscopy (SEM) where samples were mechanically polished up to  $1 \mu\text{m}$  aluminum oxide suspension followed by vibratory polishing in  $0.05 \mu\text{m}$  colloidal silica suspension to help remove residual surface strain. EBSD data processing and mapping were performed in MATLAB<sup>†</sup> using MTEX<sup>24</sup> and ATEX<sup>25</sup> was used for inverse pole figure mapping. SEM characterization was performed on a Quanta 650<sup>†</sup> FEG using secondary electron (SE) detection. Disk specimens of the AM-100 condition were prepared for scanning transmission electron microscopy (STEM) using a twinjet polisher at  $40^\circ\text{C}$  and  $10 \text{ V}$  to  $20 \text{ V}$ . The electropolishing solution was made with 10 vol% perchloric acid and methanol. The energy-dispersive x-ray spectroscopy (EDS) maps were performed on a Thermo Scientific Talos F200X<sup>†</sup> at  $200 \text{ kV}$ . Line scan data were generated using Velox<sup>†</sup> Software.

## RESULTS AND DISCUSSION

### 3.1 | Microstructure

Optical micrographs of the AM-AB sample parallel and transverse to the build direction are shown in Figure 1. The build direction has been noted in each subfigure to aid in process visualization. The darker lines in the micrographs are the melt pool tracks from the AM process. The sample exhibited an average melt pool depth of  $42.9 \mu\text{m}$  with an average melt pool width of  $54.9 \mu\text{m}$ . The AM samples show full part density across the testing area. Grain boundary mapping for the transverse direction (similar to Figure 1(b)) can be found in Figure 2(a) where HAGBs form rectangular patterns across the material. Note that the laser scanning path is rotated  $45^\circ$  in the EBSD scan compared to that of Figure 1(b). The crosshatch nature of the laser scanning strategy created a grid-like pattern of melt pool tracks where a high density of GBs form in the center of the melt pool. This is consistent with other work.<sup>26-27</sup> As shown in Figure 2(a), the transverse direction primarily consisted of HAGBs, with 81.5% of boundaries  $>15^\circ$ . It should be noted that the accurate assessment of lower angle boundaries may be undermined due to the resolution of the EBSD scan in this experiment. The  $\Sigma 3$  boundary fraction of as-built AM 316L SS in this work was significantly lower compared with other work (1.7% in this work vs. 24.8% from the work of Laleh, et al.<sup>9</sup>). With similar powder and part chemistries, the notable microstructure difference is likely attributed to the difference in process parameters. As Cr carbide nucleation is retarded on  $\Sigma 3$  boundaries, the sensitization susceptibility of AM 316L SS in this work were expected to be higher than the material used elsewhere.<sup>9</sup> Figure 2(b) shows the texture mapping with the inverse pole figure (IPF) map shown in Figure 2(c). It is evident that the transverse direction grains showed a slight preference for the  $\langle 111 \rangle$  and  $\langle 001 \rangle$  directions. From Figure 2(b), the larger (green)  $\langle 101 \rangle$  grains are interrupted by many small grains that form at the center of the melt pool.

### 3.2 | Double-Loop Electrochemical Potentiokinetic Reactivation Tests

The results of the DL-EPR tests can be found in Figure 3 to compare both AM and wrought materials under different heat-treatment conditions. Both the AM and wrought samples showed similar open-circuit corrosion potential  $E_{\text{corr}}$  at around  $-0.4 \text{ V}_{\text{SCE}}$  under all heat treatments. As the polarization moved toward an anodic direction, all AM samples presented a characteristic anodic current peak ( $i_a$ ) at approximately  $-0.175 \text{ V}_{\text{SCE}}$ .  $i_a$  increased significantly with increasing heat-treatment time, suggesting a higher dissolution rate with more

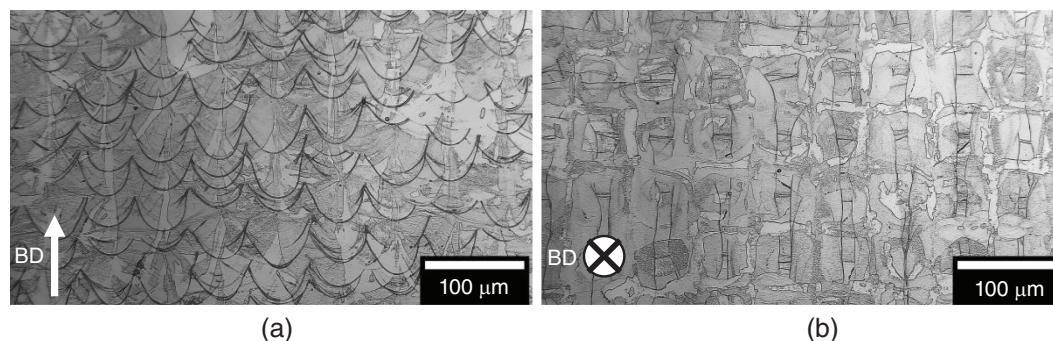


**FIGURE 1.** Optical microscopic image of the microstructure of as-built AM 316L etched with oxalic acid (a) parallel and (b) transverse to the build direction.

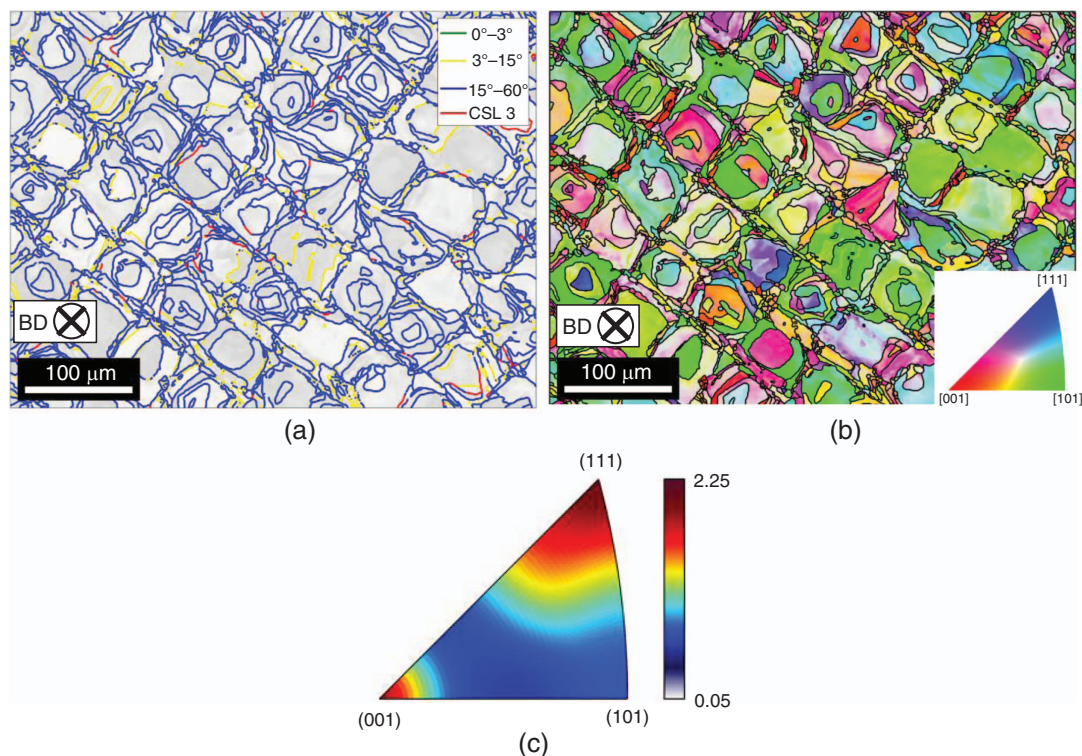


**FIGURE 2.** EBSD characterization of as-built 316L transverse to the build direction: (a) grain boundary misorientation map with melt pool visualization outlined in black, (b) grain texture orientation map, and (c) inverse pole figure showing the heat map of grain orientations.

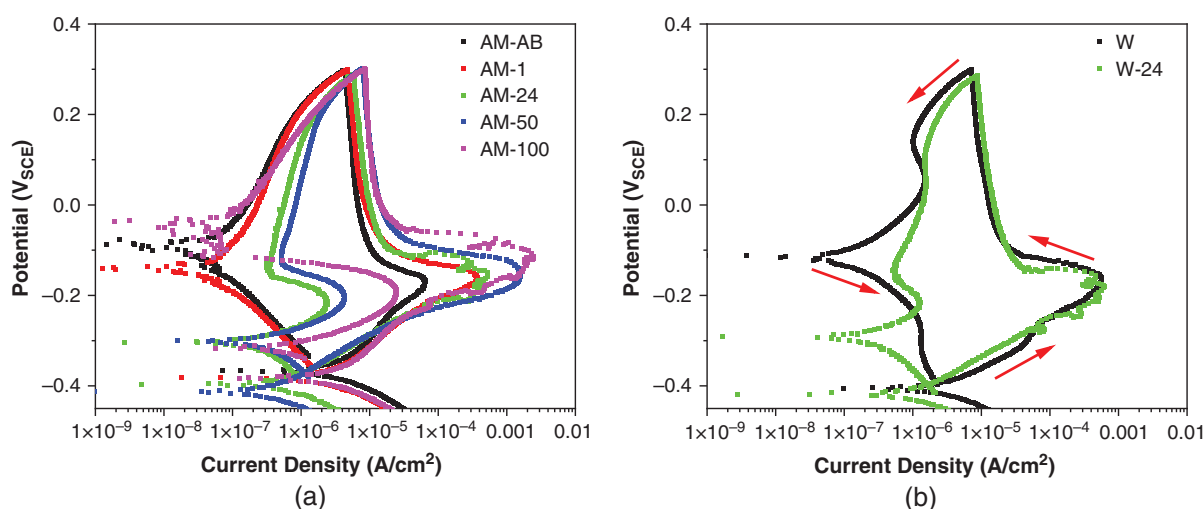


**FIGURE 3.** DL-EPR curves for (a) AM and (b) wrought samples in 0.5 M H<sub>2</sub>SO<sub>4</sub> + 0.01 M KSCN subjected to a scan rate of 1.67 mV/s with red arrows in (b) indicating the scan direction. Reactivation peaks can be observed in all samples sensitized longer than 24 h.

severe sensitization. Passivation took place in the vicinity of  $-0.1 V_{SCE}$ . A reverse scan was conducted at  $+0.3 V_{SCE}$  toward the cathodic direction. While AM-AB, AM-1, and wrought samples showed typical corrosion potential in the passivated condition, other samples presented a reactivation anodic current peak ( $i_r$ ) which indicates sensitization susceptibility.  $i_r$  increases with the sensitization time. Cr depleted region was less passivated, generally resulting in faster active dissolution.

Figure 4 summarizes the DOS as the function of sensitization time. It is important to note that a material is said to be sensitized when DOS is greater than 0.01 (1%).<sup>16</sup> An evaluation

of the 1% cutoff for determining sensitization will be discussed later. Both AM and wrought 316L SS exhibited a similar trend in DOS with time. The DOS of AM 316L SS increased with sensitization time, approaching 1% at 100 h. Desensitization<sup>28</sup> was not observed for up to 100 h. We emphasize the DOS curve in Figure 4 is flattened when approaching 100 h, which was likely caused by the full consumption of carbon from the matrix.

Figure 5 shows the optical images of the sample surface after DL-EPR study. No grain boundary attack was seen on AM-AB, AM-1, and wrought samples. Note that the straight lines found in Figure 5 are mostly polishing lines. The first signs of

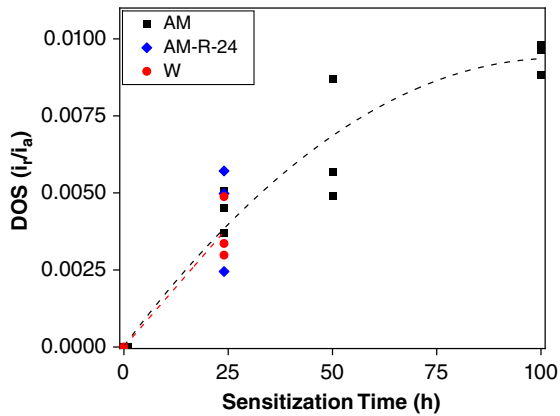


FIGURE 4. DOS of AM and wrought samples calculated from DL-EPR curves. DOS is reported as  $i_r/i_a$ .

grain boundary attack are evident at a 24-h sensitization time regardless of recovery heat treatment. As the sensitization time increased to a longer time, the resulting grain boundary attack

is greater in AM 316L SS. Wrought 316L SS does not show grain boundary attack as significant as AM 316L SS.

Comparing the DOS values of AM-24 and W-24 samples in Figure 4, there seems to be little difference (on average 0.44% and 0.37%, respectively) given that these two samples are considered unsensitized (below 1%). This conclusion is very similar to the work of Macatangay, et al.,<sup>10</sup> and contradictory to the reported work of Laleh, et al.,<sup>9</sup> in which AM 316L SS exhibited significantly fewer DOS than wrought 316L SS. Such a difference in DOS can be explained by the negligible twin fraction present in this work's AM 316L SS. Therefore, the process-to-process variation of parameters in L-PBF can lead to different corrosion responses.

### 3.3 | Intergranular Attack Susceptibility Tests (Ditching Test)

Following the practice "A" of ASTM A262,<sup>17</sup> the "ditching" test using both oxalic acid and APS was used to assess the IGC susceptibility of AM 316L SS. The microstructure of the specimens after "ditching" can be found in Figure 6. The as-built

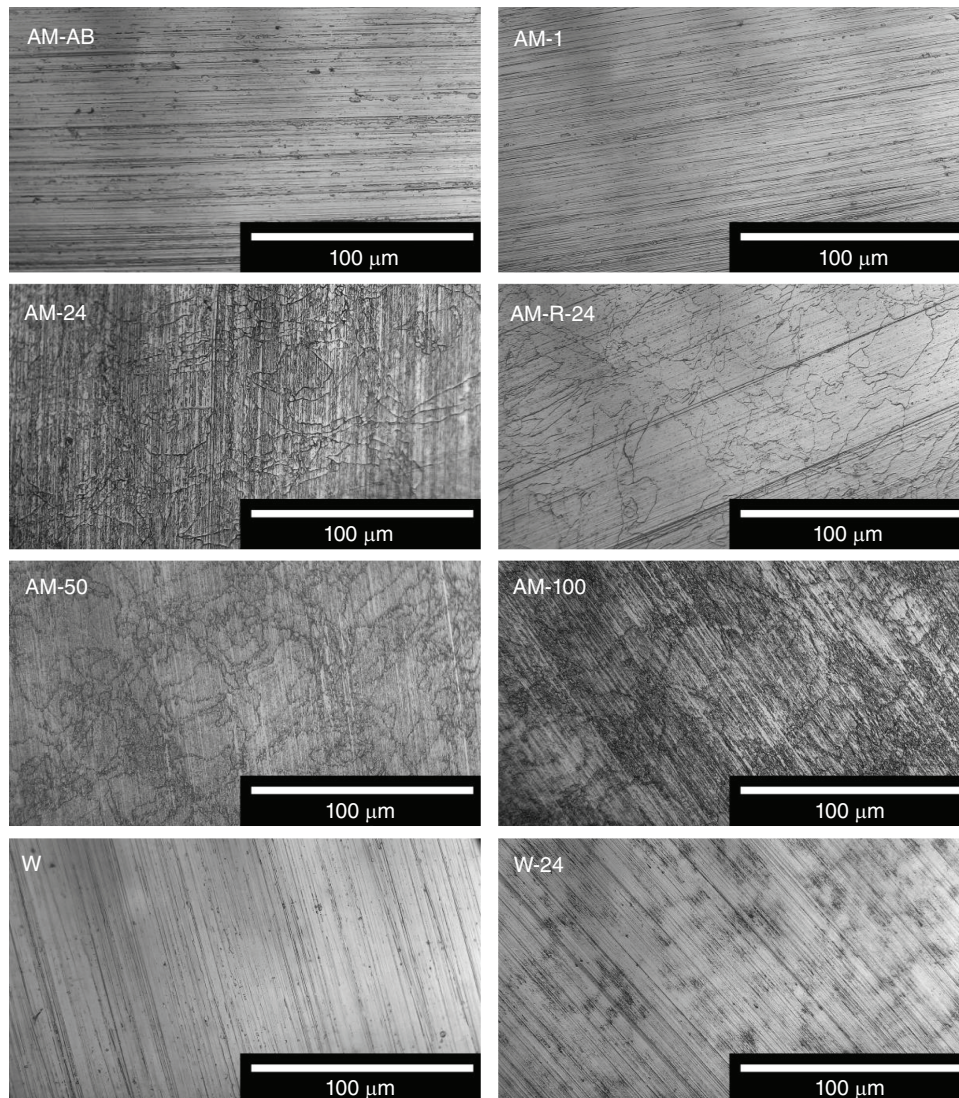
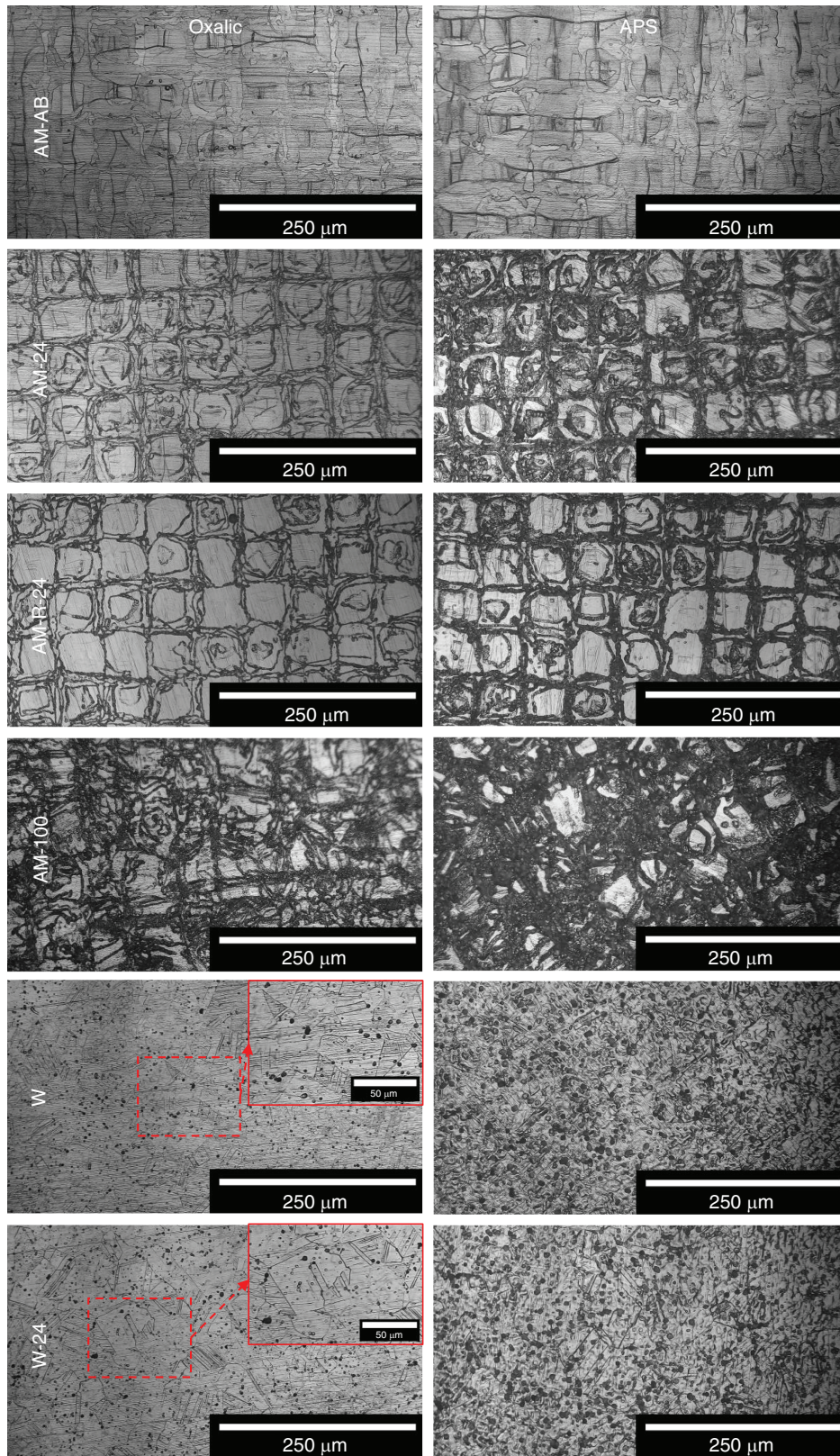


FIGURE 5. Optical microscopic images of IGC attack after the DL-EPR tests of AM and wrought materials. IGC is observed in AM 316L after sensitization longer than 24 h.



**FIGURE 6.** Optical microscopic images of AM and wrought samples after the ditching test using (left) oxalic acid and (right) ammonium persulfate. Ditching is observed in all materials sensitized longer than 24 h.

AM sample showed an attack along the melt-pool track while the HAGB presented a stepped structure, as outlined in ASTM A262.<sup>17</sup> The melt-pool attack observed will be discussed later. No pitting was observed. Note that the stepped structure is acceptable according to the standard. While the AM-1 sample was evaluated, the microstructure showed extremely similar features to the as-built condition, and as such was not included. We conclude that 1 h is not enough time to sensitize the AM sample. The AM-24 sample exhibited a ditching structure meaning sensitization has occurred, while the DL-EPR data according to ISO 12732<sup>16</sup> evaluate the material as unsensitized (Figure 4). After being subjected to 100 h of sensitization, the AM-100 sample showed significant IGC indicating Cr depletion along HAGBs due to sensitization. The nonsensitized wrought sample exhibited a stepped structure similar to the AM-AB sample, which is consistent with the DL-EPR testing. Interestingly, the wrought material showed a significant amount of end grain pitting which is seen by the dark circular features in Figure 6. This is not surprising given that austenitic SS produced by AM has been shown to have significantly higher pitting potential.<sup>29-34</sup> After sensitization for 24 h, the wrought material showed some areas of ditching with a dual structure. The results of the ditching test align with the DL-EPR test where the W-24 sample exhibited a slightly lower DOS compared to the AM-24 sample.

To further understand the response to ditching, APS was also used as a ditching solution. Samples etched with APS showed significantly more attacks as seen in Figure 6. APS is recommended for molybdenum-containing austenitic stainless steels which may show difficulty revealing step structures. However, the as-built AM and nonsensitized wrought samples showed step structures using oxalic acid indicating there was

no need to use APS for these samples. In Figure 6, one can see the significant amount of end grain pitting in the wrought samples. The end grain pits significantly hinder the evaluation of the GB attack. As such, APS may not be the best tool to evaluate IGC susceptibility in all molybdenum-containing austenitic stainless steels.

### 3.4 | Effect of Dislocation Cellular Structures on Sensitization

It has been reported that dislocation annihilation occurs within the temperature range of 800 to 1,065°C during short heat-treatment times.<sup>15,35-37</sup> In the aforementioned work, the higher-temperature range, in some cases, led to the disappearance of the cellular structures when heat treating for more than 15 min. It is important to note that at higher temperatures the formation of  $\sigma$  phase can occur leading to a multiphase material which is undesirable for the evaluation of dislocation effects on sensitization. The microstructure of the as-built and recovered samples before sensitization heat treatment can be found in Figure 7. The as-built condition shows a cellular-columnar structure where melt pool boundaries are clearly visible. After a recovery period of 10 min, dislocation annihilation occurs effectively removing the cellular structure as seen in Figure 7(d). The melt-pool boundaries are also no longer etched after the recovery treatment although some very local attack around GBs and light surface pitting occurs (bright spots shown in Figure 7(c)). This indicates that the dislocation structures have been removed and chemical homogenization has occurred while not recrystallizing the material. As such, the effects of dislocations on sensitization kinetics can be evaluated.

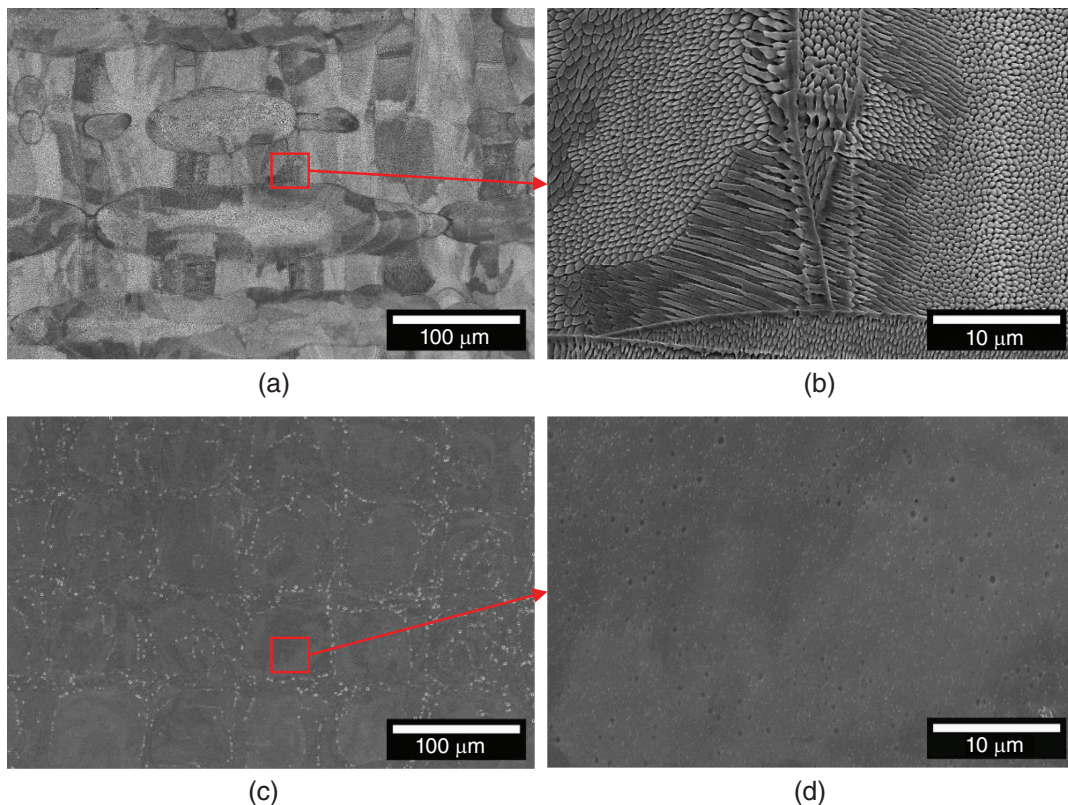


**FIGURE 7.** SEM SE image of AM (a, b) as-built showing a cellular and columnar structure and (c, d) recovered heat treatment at 1,038°C for 10 min without the cellular and columnar structure indicating a full recovery heat treatment. Both are etched in oxalic acid under similar conditions.

Investigation into the recovered and nonrecovered 24-h sensitization samples, AM-R-24 and AM-24 respectively, was performed to investigate the effects of dislocations on the sensitization kinetics of this material. After calculating the DOS for each specimen, the recovered and nonrecovered samples, on average, exhibited a DOS of 0.00438 and 0.00443, respectively, with the data points plotted in Figure 4. In Figure 6, the ditching test shows an HAGB attack that is quite comparable between the two heat-treat conditions in both oxalic acid and APS. With both conditions showing similar sensitization characteristics, the recovery heat treatment had little to no effect on sensitization kinetics. As such, the role of dislocation structures as diffusion channels for carbon and Cr seems to be minimal at best. This does not particularly align with the literature<sup>38-40</sup> where dislocations function as pipelines for carbon diffusion and significantly increase the diffusion at large depths. For wrought 316L, it has been shown that increasing dislocation density by cold work is effective at increasing DOS after low-temperature sensitization heat treatments (500°C for 264 h).<sup>40</sup> Thus, further investigation into dislocation effects on sensitization kinetics in AM 316L is warranted. It is well known that the diffusion of carbon is significantly faster than that of Cr, so one would expect the carbide precipitation kinetics to be rate limited by Cr. With the low-carbon variant of 316, there is little carbon available to form carbides, and as a result, a lower driving force for precipitation. AM 316L SS by L-PBF presented a higher amount of GBs than wrought coarse-grain 316L SS. A higher nucleation rate in AM 316L SS may accelerate carbon consumption. As carbides start forming, there is even less

carbon in the solution that is available for carbide precipitation, leading to the majority of solutionized carbon being consumed. Because there was no significant difference in DOS after a recovery heat treatment, dislocation density appears to have minimal impact on carbide precipitation. Because dislocation density plays a large role in Cr diffusion, Cr diffusion should not be concluded as the rate limiting factor. While Cr diffusion may have been slightly retarded by the recovery heat treatment, we propose the rate limiting factor for carbide precipitation of AM 316L SS is the low carbon concentration.

### 3.5 | Carbide Precipitation and Cr Depletion During Sensitization

To investigate the diffusion of elements within the samples, STEM images were taken with element maps. STEM-EDS images of the AM-100 sample are found in Figure 8 showing Cr and carbon enrichment, pointing to Cr carbide formation along HAGB. The sample sensitized for 100 h was chosen to ensure the maximum diffusion time within the scope of this study. It is important to note the higher concentration of molybdenum along the GBs as well. The Mo particles do seem to form in a semicontinuous fashion where there are areas of continuous particles interrupted by other carbides present along the boundary. EDS scans across a GB 50 nm away from carbides were performed and averaged to determine Cr depletion due to carbide formation. The average of 5 GBs scanned can be found in Figure 9(a) where one can see that the Cr concentration on average drops to 12.35 wt% due to carbide formation. Cr concentrations below 12 wt% or 13 wt% are known to make GBs

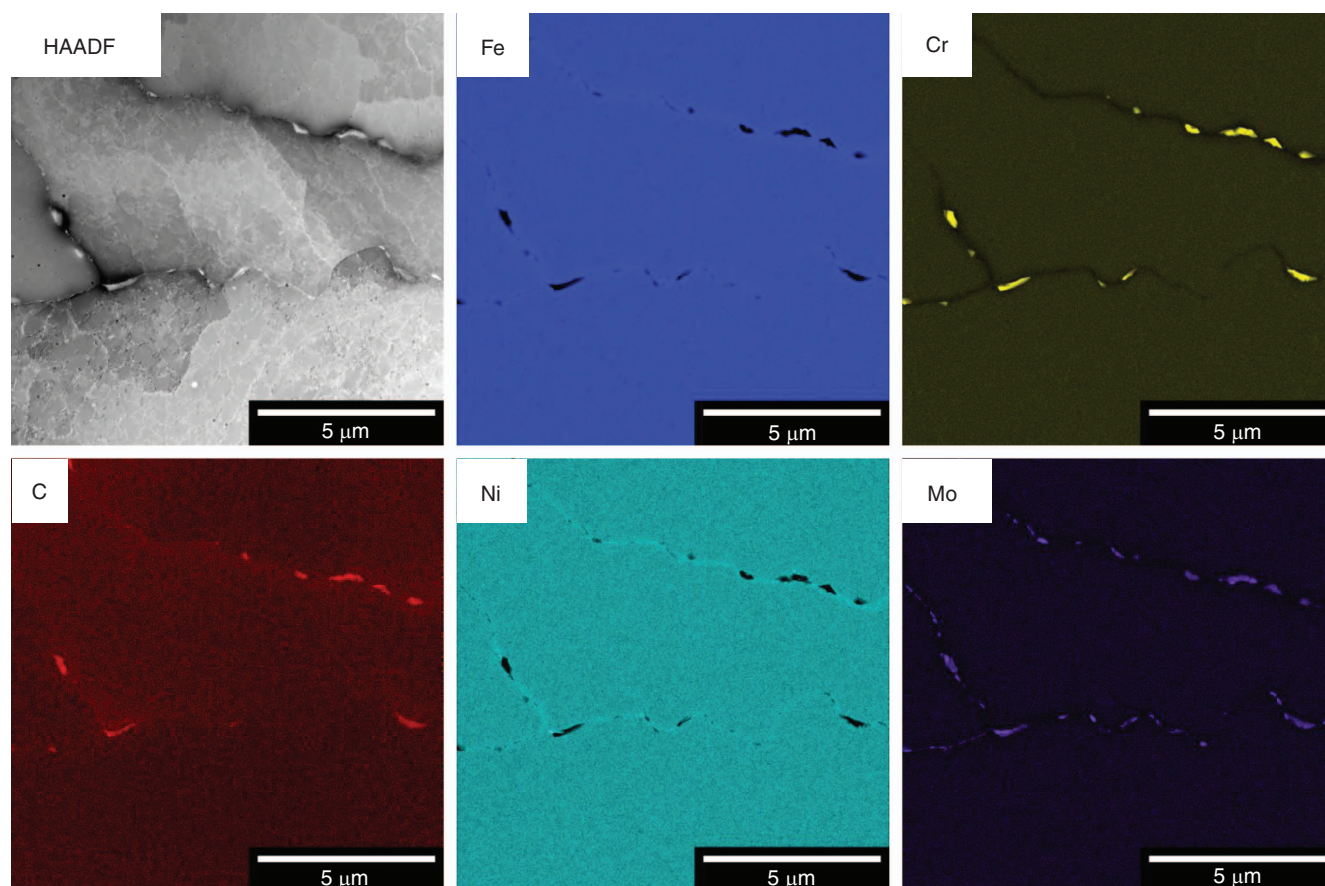


**FIGURE 8.** STEM-EDS images showing Cr carbides and Mo-rich precipitates along HAGB in AM-100. Significant Cr depletion along grain boundaries is observed.

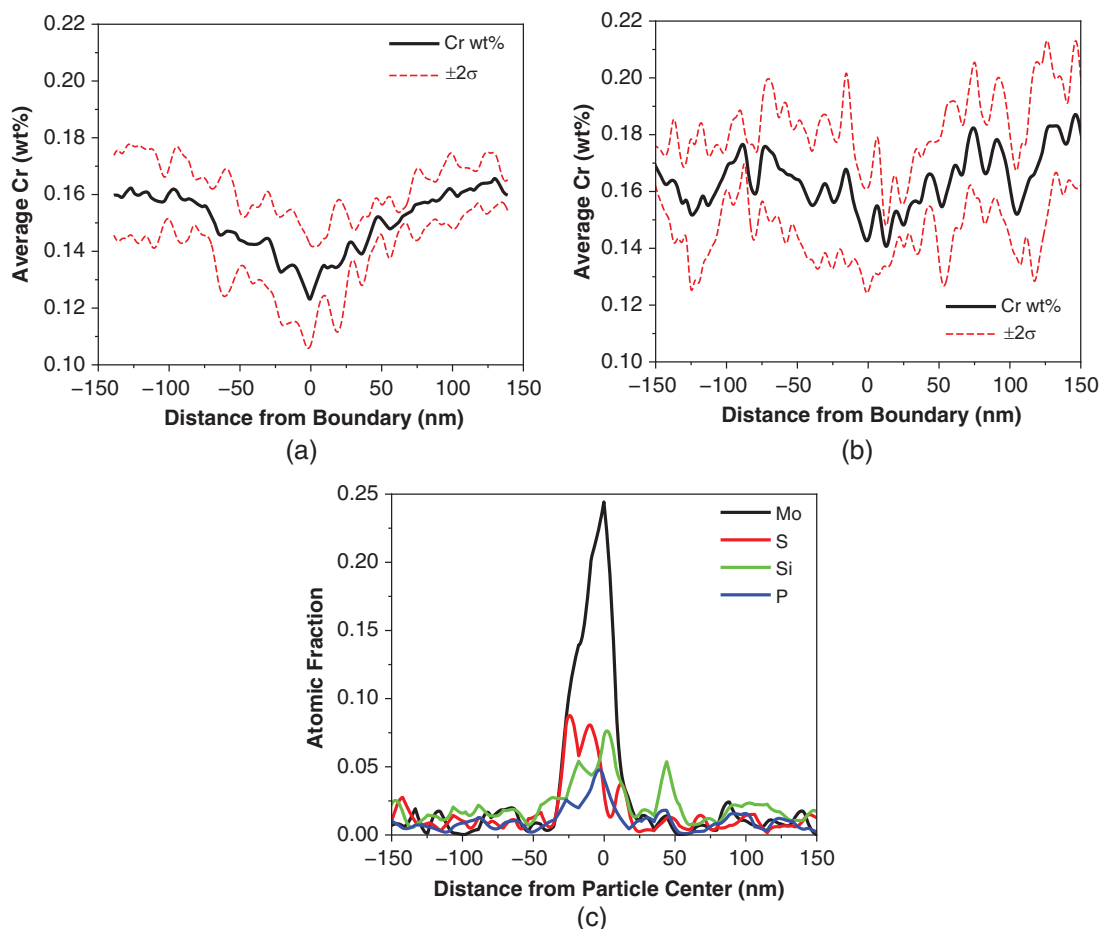


**FIGURE 9.** STEM-EDS scans of (a) 5 GBs 50 nm away from Cr carbides indicating significant Cr depletion, (b) 5 GBs far away from Cr carbides indicating slight Cr depletion, and (c) a Mo-rich particle along a GB indicating the presence of  $\text{Mo}_3\text{Si}$ .

prone to IGC,<sup>20</sup> so on average, the sample is sensitized. Looking at the  $\pm 2\sigma$  ranges in Figure 9(a), it is very possible to observe GBs with Cr levels even below 11%, which would lead to even further IGC susceptibility. This aligns well with the DL-EPR and ditching test where the AM-100 sample showed a significant IGC attack.

Investigating the Cr level at GBs far away from carbides and the Mo particles, it is seen that, in Figure 9(b), some Cr depletion occurs (dropping from approximately 17 wt% to 14 wt%). Knowing that the AM-100 sample showed significant IGC susceptibility using both testing methods, on average, GBs away from particles and carbides are generally prone to IGC. We propose the Cr wt% that makes a material prone to IGC is closer to 14 wt%. By long-time heat treatment, desensitization can happen by the back-diffusion of Cr to the depleted region. However, in this study, desensitization was not seen at the sensitization times up to 100 h. Figure 9(c) shows an EDS scan of a Mo-rich precipitate. While these precipitates originally showed high S, Si, and P levels, plotting the atomic fraction of these elements with Mo revealed that the precipitates are  $\text{Mo}_3\text{Si}$  due to the Si fraction closely following the shape of the Mo scan.  $\text{Mo}_3\text{Si}$  has been observed in other works.<sup>15</sup>

### 3.6 | Attack Modes of Double-Loop Electrochemical Potentiokinetic Reactivation and Ditching Tests

In order to assess the differences in preferential attack locations done by the two IGC tests, SEM images were taken

from the same location on a specimen after the DL-EPR and ditching tests. The AM-24 sample was subjected to the DL-EPR test first as it was previously observed that the IGC was much less severe. This would allow for less material thickness removal by repolishing, resulting in a more accurate comparison at the same location. After the DL-EPR test, an area of interest was chosen close to a specified marker and an image was taken (Figure 10[a]). One can see that the DL-EPR test attacks nearly all GBs. From this, one can conclude that the material is significantly sensitized which does not correspond with the quantitative results of the test. Contrary to some of the work of Macatangay, et al.,<sup>10</sup> no melt pool boundary or cellular structure attack was observed. Additionally, the DL-EPR test shows a selective dissolution of the passive film. As the surface oxide film is also attacked in the DL-EPR tests, the reactivation peak current is not entirely dependent on IGC. As a result, the DOS value may be overestimated.

Once the DL-EPR SEM images were taken, the sample was ground until no optical evidence of GB attack was present, further ground in accordance with *Intergranular Attack Susceptibility (Ditching Test)* section, and tested using oxalic acid ditching. The area of interest was found and SEM images were taken (Figure 10[b]). One can see that the grains do not exactly mirror the ones found in the DL-EPR test which is likely due to the material removal by grinding. As seen in Figure 10(b), the ditching test significantly attacks the GBs and induces pitting. Because the ditching test is a current-controlled test, the sample

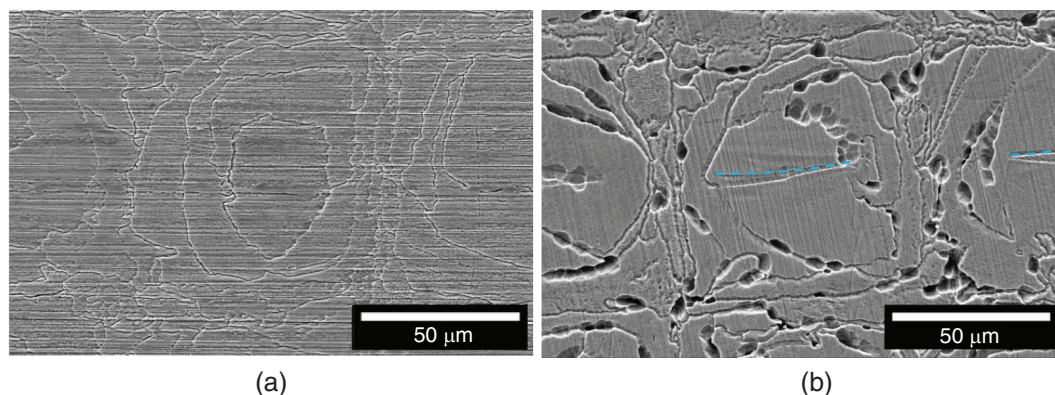


**FIGURE 10.** SEM SE images of AM-24 subjected to a (a) DL-EPR test where GB attack is observed and (b) ditching test using oxalic acid where GB and melt pool boundary attack is observed. Some melt pool boundaries in (b) are marked in blue. Images were taken in the same area using distance control from a specified spot outside the image capture area.

may have varying electrical potentials which could result in a potential being high enough to cause pitting. Interestingly, some melt-pool boundary attacks (blue lines in Figure 10[b]) can also be seen in the ditching test which is not present in the DL-EPR test. An important conclusion from this work is that both tests are attacking the GBs of the sensitized AM 316L SS, and the attack using the ditching test are more severe.

### 3.7 | Perspectives on the Testing Methodology of Sensitization for AM 316L SS

The AM-100 sample was on average considered non-sensitized by STEM work (Figure 9[a]) by the traditional 12 wt% Cr rule<sup>20</sup> but statistically showed some boundaries will be sensitized below 12 wt%. This fundamental, quantitative approach of determining sensitization provides great insight to assess other more time-conscious approaches such as the DL-EPR and ditching tests. An important distinction should be made that the DL-EPR test did not reveal melt pool boundaries in the AB and AM-1 conditions. Therefore, the DL-EPR test evaluates material for IGC regardless of it being AM or wrought. The quantitative results of the DL-EPR test (Figure 4) for the 700°C 100-h condition indicated the material as nearly sensitized which corresponds well to the STEM work performed where Cr depletion occurs and can statistically reduce GB Cr levels below 12 wt%. Any sample sensitized at 24 h or longer also qualitatively showed an IGC attack (Figure 5) which is contradictory to the quantitative results that evaluated the samples as nonsensitized. With IGC being seen after 24-h sensitization time, samples tested should be microstructurally evaluated in addition to calculating DOS. This does raise a question: if there is IGC even when the DOS is below 1%, should the material pass even if IGC is present? It is imperative to not jump to conclusions about the IGC susceptibility based on one point of data but to use as many characterization tools as possible to fully evaluate the material. On the positive side, the DL-EPR test evaluated the DOS as increasing with sensitization time which is consistent with the microstructural features. The combination of the benefits manifests the DL-EPR test as a prime candidate for IGC evaluation of AM and wrought austenitic SS, although ISO 12732<sup>16</sup> considering a DOS of 1% to be sensitized may not provide a full picture of IGC susceptibility. As such, further work should be performed to develop a DL-EPR standard that takes the potentiodynamic response and microstructural features into account.

Sensitization evaluation using the ditching test of ASTM A262<sup>17</sup> could present some complications when

evaluating austenitic SS produced by AM. In this work, as-built samples showed heavy melt-pool boundary attacks with stepped GBs. The initial thought would be to fail the material, but further investigation into melt-pool attacks is required. Godec, et al.,<sup>41</sup> found slight Cr and Mo depletion along melt pool boundaries (17.4 wt% to 16.6 wt% and 4.2 wt% to 3.1 wt%, respectively) in AM 316L SS in the as-built condition. The slight reduction in Cr along the melt pool boundary would explain the preferential etching phenomenon. Sommer, et al.,<sup>42</sup> argued that melt pool boundaries could be etched due to chemical segregation or changing solidification modes from a cellular to planar form. With this in mind, melt pool boundary etching should not be characterized as sensitization using the ditching test because the elemental segregation is not significant enough to promote IGC and carbide formation does not occur. Performing the ditching test does reveal stepped GBs in the AB condition, which is consistent with its wrought counterpart, however, the deep etching of melt pool boundaries may lead some to fail the sample unjustly. As the sensitization time increased to 24 h and beyond, the ditching test revealed the GBs as susceptible to IGC, and significant pitting was also observed. From this change in preferential attack location, one could conclude that sensitization treatment was significant enough to promote sensitization. Observing IGC in samples sensitized for 24 h and beyond is consistent with the DL-EPR test, although the GBs in the ditching test are qualitatively attacked more (Figures 5, 6, and 10). While an advantage of the ditching test is its ability to quickly screen a material, AM austenitic SS samples require more complex analysis of different microstructural features. ASTM A262<sup>17</sup> would, therefore, need to be updated for AM austenitic SS to include melt pool attack in addition to the normal GB classification. Because the ditching test does not only test the GBs, and, as a result, evaluators must use a more subjective evaluation method, the DL-EPR test seems to be a more promising testing method for AM austenitic SS for sensitization.

### CONCLUSIONS

> Sensitization heat treatments at 700°C for various times up to 100 h were performed on AM and wrought 316L SS. In order to evaluate the DOS, the DL-EPR and ditching tests were performed on all samples. This work also investigated the role of dislocation cellular structures on the precipitation kinetics of Cr carbides and the Cr depletion along GBs after 100 h of sensitization in AM 316L SS.

- The DL-EPR can be used to detect IGC susceptibility in AM 316L SS. Melt-pool boundary and cellular structure were not attacked by a DL-EPR test, but selective surface oxide dissolution was present. The quantitative results of the DL-EPR test are a useful tool to evaluate DOS between samples, but post-test microstructural characterization should be performed to evaluate IGC attack. The DL-EPR test should be updated to provide a more nuanced determination of sensitization that includes microstructural evaluation rather than solely relying on the 1% rule. The DL-EPR test reactivation peak current does not rely only on IGC but also surface oxide dissolution which may lead to overestimating DOS.
- The ditching test can be used to detect IGC susceptibility in AM 316L SS as well. A significant melt-pool boundary attack was observed. The use of APS is generally used for Mo-containing steels, but the attack observed was much more significant compared to the oxalic acid. This could make post-test microstructural characterization challenging. The qualitative results of the ditching test provide a subjective qualification protocol. As the melt-pool boundaries do not have enough Cr depletion to cause IGC, the ditching test should be updated to inform evaluators that melt-pool boundaries should not be considered ditching structures.
- The minimum time for sensitization peaks to occur during a DL-EPR test is between 1 h and 24 h. This correlates well with the microstructural results of the DL-EPR and ditching tests. There is minimal difference in the DOS between AM and wrought 316L in this work.
- A recovery heat treatment of 1,038°C for 10 min was effective in promoting dislocation annihilation without promoting recrystallization. As a result, the recovered condition does not show a cellular structure. Recovery heat treatment had little to no effect on DOS and IGC resistance which is likely due to the low carbon level in AM 316L SS rather than Cr diffusion. As such, dislocation density likely has little effect on sensitization kinetics in AM 316L.
- Cr carbide precipitation and HAGB Cr depletion are present in AM 316L where the depletion reached 12.35 wt% on average after 100 h of sensitization at 700°C. GBs away from carbides exhibited 14 wt% Cr which were prone to IGC, thus the Cr wt% that makes a material prone to IGC is close to 14 wt% in contrast to 12 wt%.

## ACKNOWLEDGMENTS

The experimental work was primarily supported by The U.S. Nuclear Regulatory Commission (NRC) under Grant No. NRC-313100-21-M-0047. TEM characterization was supported by Dr. Miao Song (University of Michigan) through the Idaho National Laboratory's Laboratory Directed Research & Development (LDRD) Program under the U.S. Department of Energy (US DOE)'s Idaho Operations Office Contract No. DE-AC07-05ID14517. J. Snitzer also thanks the support from the University Nuclear Leadership Program (UNLP) Graduate Fellowship by the Office of Nuclear Energy, The U.S. Department of Energy. This material is based upon work supported under a Department of Energy, Office of Nuclear Energy, University Nuclear Leadership Program Graduate Fellowship.

## References

1. T. DebRoy, H.L. Wei, J.S. Zuback, T. Mukherjee, J.W. Elmer, J.O. Milewski, A.M. Beese, A. Wilson-Heid, A. De, W. Zhang, *Prog. Mater. Sci.* 92 (2018): p. 112-224.
2. V.B. Vukjum, R.K. Gupta, *Mater. Des.* 221 (2022): p. 110874.
3. R. Casati, J. Lemke, M. Vedani, *J. Mater. Sci. Technol.* 32 (2016): p. 738-744.
4. X.X. Yao, P. Ge, J.Y. Li, Y.F. Wang, T. Li, W.W. Liu, Z. Zhang, *Comput. Mater. Sci.* 182 (2020).
5. M. Gor, H. Soni, V. Wankhede, P. Sahlot, K. Grzelak, I. Szachgluchowicz, J. Kluczyński, *Materials* 14, 21 (2021): p. 6527.
6. J.J. Lewandowski, M. Seifi, *Annu. Rev. Mater. Res.* 46 (2016): p. 151-186.
7. C. Wang, X. Tan, E. Liu, S.B. Tor, *Mater. Des.* 147 (2018): p. 157-166.
8. D.A. Macatangay, S. Thomas, N. Birbilis, R.G. Kelly, *Corrosion* 74 (2017): p. 153-157.
9. M. Laleh, A.E. Hughes, W. Xu, N. Haghdadi, K. Wang, P. Cizek, I. Gibson, M.Y. Tan, *Corros. Sci.* 161 (2019): 108189.
10. D.A.T. Macatangay, J.M. Conrades, K.L. Brunner, R.G. Kelly, *Corrosion* 78, 1 (2022): p. 13-24.
11. J. Yang, X. Liu, M. Song, L. He, S. Bankson, M. Hamilton, B. Prorok, X. Lou, *Addit. Manuf.* 50 (2022): 102547.
12. F.P. de Moraes, S.F. Alves, R.L. Plaut, A.F. Padilha, *Proc. Struct. Integrity* 17 (2019): p. 131-137.
13. E.A. Trillo, L.E. Murr, *J. Mater. Sci.* 33 (1998): p. 1263-1271.
14. A.F. Padilha, D.M. Escriba, E. Materna-Morris, M. Rieth, M. Klimenkov, *J. Nucl. Mater.* 362 (2007): p. 132-138.
15. H. Yin, M. Song, P. Deng, L. Li, B.C. Prorok, X. Lou, *Addit. Manuf.* 41 (2021): 101981.
16. ISO 12732, "Corrosion of Metals and Alloys—Electrochemical Potentiokinetic Reactivation Measurement Using the Double Loop Method (based on Cihal's method)" (Geneva, Switzerland: ISO, 2006).
17. ASTM A262, "Standard Practices for Detecting Susceptibility to Intergranular Attack in Austenitic Stainless Steels" (West Conshohocken, PA: ASTM International, 2015).
18. R.B. Rebak, S.W. Dean, *Corrosion* 76 (2020): p. 742-749.
19. R.V. Taiwade, A.V. Ingle, R.K. Khatirkar, *ISIJ Int.* 54 (2014): p. 1898-1905.
20. H. Sidhom, T. Amadou, H. Sahlaoui, C. Braham, *Metall. Mater. Trans. A Phys. Metall. Mater. Sci.* 38 (2007): p. 1269-1280.
21. G. Liu, Y. Liu, Y. Cheng, J. Li, Y. Jiang, *Materials* 12 (2019): 1385.
22. C. Man, Z. Duan, Z. Cui, C. Dong, D. Kong, T. Liu, S. Chen, X. Wang, *Mater. Lett.* 243 (2019): p. 157-160.
23. U.K. Mudali, R.K. Dayal, J.B. Gnanamoorthy, P. Rodriguez, *Metall. Mater. Trans. A* 27 (1996): p. 2881-2887.
24. R. Hielscher, C.B. Silbermann, E. Schmidla, J. Ihlemann, *J. Appl. Crystallogr.* 52 (2019): p. 984-996.
25. B. Beausir, J.-J. Funderberger, *Analysis Tools for Electron and X-ray Diffraction*, ATEX: software, Université de Lorraine, Metz, 2017, [www.atex-software.eu](http://www.atex-software.eu).
26. O. Andreau, I. Koutiri, P. Peyre, J.D. Penot, N. Saintier, E. Pessard, T. de Terris, C. Dupuy, T. Baudin, *J. Mater. Process. Technol.* 264 (2019): p. 21-31.
27. A.A. Antonysamy, J. Meyer, P.B. Prangnell, *Mater. Charact.* 84 (2013): p. 153-168.
28. A. Tekin, J.W. Martin, B.A. Senior, *J. Mater. Sci.* 26 (1991): p. 2458-2466.
29. Q. Chao, V. Cruz, S. Thomas, N. Birbilis, P. Collins, A. Taylor, P.D. Hodgson, D. Fabijanic, *Scr. Mater.* 141 (2017): p. 94-98.
30. J. Chen, Q. Xiao, H.B. Lee, C. Jeong, K. Jang, C. Jang, *npj Mater. Degrad.* 6 (2022): 33.
31. M.A. Melia, H.D.A. Nguyen, J.M. Rodelas, E.J. Schindelholz, *Corros. Sci.* 152 (2019): p. 20-30.
32. R.F. Schaller, A. Mishra, J.M. Rodelas, J.M. Taylor, E.J. Schindelholz, *J. Electrochem. Soc.* 165 (2018): p. C234-C242.
33. G. Sander, S. Thomas, V. Cruz, M. Jurg, N. Birbilis, X. Gao, M. Brameld, C.R. Hutchinson, *J. Electrochem. Soc.* 164 (2017): p. C250-C257.
34. M. Kazemipour, M. Mohammadi, E. Mfoumou, A.M. Nasiri, *JOM* 71 (2019): p. 3230-3240.
35. P. Krakhmalev, I. Yadroitsava, G. Fredriksson, I. Yadroitsev, *South Afr. J. Ind. Eng.* 28 (2017): p. 12-19.
36. T. Voisin, J.B. Forien, A. Perron, S. Aubry, N. Bertin, A. Samanta, A. Baker, Y.M. Wang, *Acta Mater.* 203 (2021).
37. P. Krakhmalev, G. Fredriksson, K. Svensson, I. Yadroitsev, I. Yadroitsava, M. Thuvander, R. Peng, *Metals* 8, 8 (2018): p. 643.

38. K. Lu, C.F. Huo, Y. He, J. Yin, J. Liu, Q. Peng, W.P. Guo, Y. Yang, Y.W. Li, X.D. Wen, *J. Phys. Chem. C* 122 (2018): p. 23191-23199.
39. A.F. Smith, *Met. Sci.* 9 (1975): p. 375-378.
40. V. Kain, K. Chandra, K.N. Adhe, P.K. De, *J. Nucl. Mater.* 334, 2 (2004): p. 115-132.
41. M. Godec, S. Zaefferer, B. Podgornik, M. Šinko, E. Tchernychova, *Mater. Charact.* 160 (2020): 11074.
42. K. Sommer, L. Agudo Jácome, R. Hesse, D. Bettge, *Adv. Eng. Mater.* 24 (2022): 2101699.